Structural, morphological, optical and dielectric investigations in cobalt doped bismuth ferrite nanoceramics prepared using the sol-gel citrate precursor method

Waseem Ahmad Wani [a], Souvik Kundu [b], Kannan Ramaswamy [a], Harihara Venkataraman [a], [*]

[a] Department of Physics, BITS−Pilani, Hyderabad Campus, Jawahar Nagar, Kapra Mandal, Medchal District, Hyderabad, Telangana, 500078, India
[b] Department of Electrical Engineering, BITS−Pilani, Hyderabad Campus, Jawahar Nagar, Kapra Mandal, Medchal District, Hyderabad, Telangana, 500078, India

ARTICLE INFO

ABSTRACT

In this work, the synthesis of un-doped and cobalt (Co)-doped nanoceramic samples of bismuth ferrite by cost-effective sol-gel citrate precursor technique are presented. Detailed investigations have been attempted to study the effect of Co substitution on the structural, morphological, dielectric and optical properties of bismuth ferrite prepared using the citrate precursor method. The main feature of these investigations is the relative elimination of secondary phase formation while preparing bismuth ferrite nanoceramic samples. X-ray diffraction analysis shows distorted rhombohedral perovskite structure for all compositions of $BiFe_{1−x}Co_xO_3$ (x = 0.00, 0.03, 0.05, 0.10) nanoceramics, where the average crystallite size and induced strain in these samples are calculated using Scherrer's method and Williamson−Hall equation, respectively. An increasing trend of average crystallite size with increase in dopant concentration was observed. Microstructural examinations of pure and doped BFO identified compact granular shaped microstructures with irregular size and shape but changed to uniform spherical shape after Co substitution up to 10 mol%. Confirmation of the uniform distribution of dopants throughout the sample has been carried out using elemental mapping studies. On the other hand, the chemical states of all the constituent elements were identified by X-ray photoelectron spectroscopic studies. Non-monotonic variations in the real part of dielectric values were observed with increasing Co concentrations. The optical absorption coefficient was found to increase by 35% in 10 mol% Co-doped BFO than that of pure BFO at 480 nm. Optical band gap studies depicted a striking inverse correlation of bandgap values and doping concentration up to 10 mol% Co substitution without varying the intrinsic structural feature of bismuth ferrite. Interestingly, the bandgap value of bismuth ferrite was varied from (2.08 ± 0.02) eV to (1.63 ± 0.02) eV, in the visible region. The results from present investigations suggest that synthesis techniques and chemical substitution need to be continuously optimized to get desired physical properties suitable for device applications such as photovoltaics.

© 2020 Elsevier B.V. All rights reserved.

1. Introduction

Bismuth ferrite (BFO), being a distinctive multiferroic material, has seen an upsurge in the scientific community globally due to its fascinating electronic, physical and optical properties. BFO belongs to the *R3C* space group and has distorted rhombohedral perovskite structure (ABO_3) with Bi atom at A site and Fe atom at B site. BFO exhibits ferroelectric and G-type anti-ferromagnetic orders at room temperature, which makes it a potential candidate for magneto-electric device applications [1–6]. Besides, it shows some other unique features, including large remnant polarization (90 μC/cm^2), high Curie temperature (T_C ~ 1103 K), high Néel temperature ($T_Ñ$ ~ 643 K), piezoelectricity and switchable photo-current [5,6]. Apart from these physical and electronic properties, BFO exhibits significant optical absorption in the visible range of the spectrum. These features make it a suitable material for multifunctional device applications. Despite these favorable properties, the difficulty in

* Corresponding author.
E-mail address: hari@hyderabad.bits-pilani.ac.in (H. Venkataraman).

synthesizing the pure phase of BFO combined with a high leakage current density hinders its potential for practical device applications [7]. The high leakage current density is due to the existence of oxygen vacancies and variable oxidation states of Fe ion.

Furthermore, the volatile nature of Bi generates A—site vacancies (V_{Bi}^{3-}) in the crystal lattice, which could lead to either the creation of the impurity phase or the formation of more oxygen vacancies. Therefore, various methods are employed to reduce the leakage current density by doping the B sites (in BFO) with transition metals such as Mn, Cr, and Ti [7–13]. Substitution of isovalent (such as Mn, Cr) and aliovalent (such as Ti) elements at B site has proved an efficient way to reduce the leakage current density [14]. The charge compensation in high valence dopant is achieved by either filling the oxygen vacancies, creation of cationic vacancies or decrease of cationic valence. On the other hand, the substitution of low valence elements also requires charge compensation, which is satisfied by either the creation of anion (oxygen) vacancies or by an increase in cationic valence ($Fe^{2+}-Fe^{3+}$) and hence inhibit the valence fluctuation of Fe^{3+} to Fe^{2+} [14,15]. Thus low valence dopants tend to create more oxygen vacancies, which result in bandgap reduction due to defect induced levels within bandgap or increase in density of states. The low valence (2+) ion substitution also paves the possibility for the creation of defective dipoles hence can result in a drastic change in various physical properties.

The last several decades have seen tremendous improvements in the area of photovoltaics in terms of new materials and cost reduction due to better light management and overall efficiency improvement. Nevertheless, commercialized photovoltaics are not yet cost-competitive compared to fossil fuels owing to sophisticated fabrication techniques or scarce solar material used. In this context, ferroelectric materials may provide an alternate pathway towards the next generation photovoltaics with a new mechanism of charge transport based on induced depolarization field. These materials show various other fascinating features beneficial for photovoltaic, which includes (i) cost-effective fabrication process (ii) bulk based photovoltaic effect and, (iii) unusual photovoltaic effect. However, the visible light-harvesting capability of these materials is still challenging, mainly due to the larger bandgap (typically more than 3 eV). Among various ferroelectric materials, BFO has gained attention towards photovoltaic applications owing to its relatively lower bandgap (<2.70 eV).

Furthermore, photovoltaic materials must have a significant absorption coefficient in the visible spectrum to absorb maximum solar irradiation. In this aspect, normally, due to its higher bandgap, the BFO does not absorb light compared to other conventional inorganic photovoltaic materials like Si, and the light absorption shows rapid decrement beyond 500 nm. To circumvent this, several research groups have attempted chemical substitution in A and B sites of BFO and have shown enhanced light absorption in the wavelength range from 500 nm to 800 nm. In these investigations, substitutions of several dopants like Zn, Cu, Ni, Co, Cr, Mn, and Ho appeared to reduce the optical bandgap of BFO [16–19]. However, several research groups have reported structural phase transitions from rhombohedral to orthorhombic with chemical substitution. Recently, Rhaman et al. reported significant bandgap reduction in orthorhombic BFO via Co substitution [18].

Interestingly, chemical substitution has improved the phase formation. However, a complete exemption from secondary phases is difficult to achieve due to the kinetics of formation. Therefore, tailoring optical bandgap in BFO without deteriorating the crystal structure and pure phase formation is still a key challenge. Both these are critical aspects for BFO to be considered as a potential photovoltaic material.

Several methods have been attempted to obtain a pure phase of BFO material. These include the hydrothermal method, solid-state

reaction method, liquid phase sintering, microwave hydrothermal method, sol-gel method and citrate precursor method among several other techniques [20–26]. Among all these mentioned techniques, sol-gel method has got attention owing to reasonable control on atomic level distribution, low synthesis temperature, and low-cost process. However, synthesizing a single phase of BFO is still a key challenge due to the volatile nature of bismuth. To overcome this limitation, several research groups have used 3% to 10% excess of bismuth to compensate for the bismuth loss due to volatilization. Meanwhile, the reported sol-gel synthesis approaches using ethylene glycol, 2-methoxyethanol, and water as solvents (with excess and without excess Bi), have yielded secondary phases along with pure BFO.

To the best of our knowledge, the sol-gel citrate precursor method using water as the solvent has not been used in the earlier investigations to synthesize the Co-doped BFO nanoceramic samples at lower annealing temperature(550 °C). In particular, the X-ray characterization of the samples prepared using this method exhibit fewer impurity peaks compared to a recent attempt by another research group where the authors have synthesized Co-doped BFO using ethylene glycol as a solvent [18]. Additionally, there is no much detailed investigation on Co-doped BFO nanoceramics reported in literature so far. Encouraged by the observations of a relatively pure phase of BFO and Co-doped BFO in our present work, we report here a detailed investigation on the structural, compositional, morphological, dielectric and optical properties of these nanoceramics.

2. Experimental section

2.1. Synthesis

Several methods exist to synthesize BFO. However, preparing BFO without the appearance of secondary phases is unavoidable due to the kinetics of the formation of BFO. Various other factors also determine the pure phase formation of BFO, which includes multiple oxidation states of Fe ion, volatile nature of Bi at higher temperatures and oxygen ion vacancies as mentioned earlier. Conventional solid-state reaction route is usually preferred to prepare BFO ceramics [27]. Several other techniques also exist to make pure BFO including sol-gel method, co-precipitation method, hydrothermal method, liquid phase sintering method and citrate precursor method [28–32]. Among these various methods, sol-gel technique is a cost-effective and straightforward way for preparing nanopowders and thin films of BFO with tunable particle shape and particle size. The synthesis technique used in these investigations, namely the sol-gel citrate precursor technique, is described below.

In the current investigations, $BiFe_{1-x}Co_xO_3$ (x = 0.00, 0.03, 0.05, 0.10) nanoceramic samples were synthesized. In the present synthesis, the precursors are of analytical grade and therefore do not need further purifications. The starting materials for the preparation are bismuth nitrate pentahydrate ($Bi(NO_3)_3.5H_2O$), ferric nitrate nonahydrate ($Fe(NO_3)_3.9H_2O$), cobalt nitrate hexahydrate ($Co(NO_3)_2.6H_2O$), citric acid ($C_6H_8O_7$), nitric acid (HNO_3) and distilled water. First, the stoichiometric weights of ($Bi(NO_3)_3.5H_2O$), ($Fe(NO_3)_3.9H_2O$), and $Co(NO_3)_2.6H_2O$ were dissolved in distilled water. A chelating agent, citric acid, is added to the above mixture, and the ratio of citric acid to metal salts is 2:1. A few drops of nitric acid helps in controlling the hydrolysis rate. The entire solution was vigorously stirred on a magnetic stirrer until the appearance of homogeneous sol. The resultant sol was heated at 80 °C for 12 h under a constant stirring rate to get a gel deposit. The gel-deposit was dried at 120 °C and a fluffy residue was obtained. The fluffy residue was then ground using pestle and mortar and the fine powder was extracted. Subsequently, the fine powder was

calcined at 400 °C for 2 h. The calcined powder was ground again and mounted into cylindrical pellets of desired thickness and 10 mm diameter. Finally, the pellets were sintered at 550 °C for 2 h. The whole experimental process was performed under ambient atmospheric, and the heating rate (4 °C/min) was kept constant throughout the synthesis. The densified pellets were polished on both sides with silver paste for dielectric measurements.

2.2. Material characterization

The crystal structure of prepared samples was examined by X-ray diffractometer (XRD) (Rigaku Ultima-IV) over a 2θ range of 20−70° using Cu Kα radiation. The chemical valence of the prepared samples was determined by X-ray photoelectron spectroscopy (Thermo Scientific K-Alpha). The morphological features and chemical composition of these samples were characterized by using a field emission scanning electron microscope (FESEM, FEI-Apero LoVac) associated with energy dispersive X-ray spectroscopy (EDAX). UV−vis spectrophotometer (JASCO V−670) was used to record the absorption spectra and Tauc's method used to calculate the optical bandgap of all these samples.

2.3. Dielectric measurements

To carry out the dielectric studies, the pellets were silver pasted on both surfaces and dried at 60 °C for about 30 min. The room temperature dielectric measurements were carried out on these pellets as a function of frequency using Wayne Kerr LCR meter with signal strength of 1 V_{rms}.

3. Results and discussions

3.1. XRD studies

The initial investigation on the formation of different phases and structural characterization was carried out by XRD. Fig. 1(a) shows the XRD patterns of the $BiFe_{1−x}Co_xO_3$ in the un-doped sample and Co-doped nanoceramic samples with doping concentrations of 3 mol%, 5 mol%, and 10 mol%. The XRD pattern in all the samples shows a distorted rhombohedral perovskite structure of BFO. The XRD data agrees with the JCPDS data file (PDF#861518) of BFO. Traces of secondary peaks that belong to the impurity phase of $Bi_2Fe_4O_9$ were also detected which is marked as a hash sign in Fig. 1(a).

Furthermore, the XRD patterns reveal that there is no significant influence on the structural properties due to chemical substitution with cobalt. This result signifies that BFO retains the rhombohedral structure despite doping up to 10 mol% of Co atom, which might be attributed to comparable radii difference of Fe^{3+}(0.645 Å) and Co^{2+}(0.745 Å) ions. However, a further increase in Co concentration (20 mol%) resulted in prominent impurity peaks, as depicted in Fig. 1(b). The enlarged view of (104) and (110) peaks, as illustrated in Fig. 1(c) shows the shift of peaks as well as variation in peak widths. In particular, the (104) and (110) peaks shifted by 0.24° towards the lower 2θ values for Co doping of 3 mol%. However, with higher doping concentrations, the peak shift does not show a linear variation. The change of the XRD peaks can be attributed to particle size variation and crystal distortion as a result of a difference in ionic radii of the dopant and host matrix site ion. Nevertheless, the rhombohedral structure of the crystallites remains unchanged as per our XRD data. In a recent publication on Co-doped BFO the authors have reported structural phase change to orthorhombic [18].

Analysis of the XRD data using Debye-Scherrer equation (given in Eqn. (1)) yielded a mean crystallite size in the range from 43 nm to 49 nm.

$$D = \frac{k\lambda}{\beta cos\theta} \qquad (1)$$

where D is the particle size, k is a constant shape (spherical) factor (~0.9), β is the peak width intensity, λ is the wavelength of radiation source (~1.5406 Å for CuK_α source) and θ is the peak position. The crystallite size with Co substitution at the Fe site of BFO increased with increasing doping concentration, as depicted in Fig. 1(d). The increase in the size of the crystallite could be due to the larger ionic radius of Co^{2+} (0.745 Å) ion in comparison to Fe^{3+} (0.645 Å) ion. Furthermore, peak broadening can also occur due to strain-induced by crystal distortion. Therefore, XRD peak widths were analyzed using Williamson−Hall method, which could separate the contribution to the peak width arising from both crystallite size and strain. The corresponding equations are provided [33]:

$$\beta = \beta_{strain} + \beta_{size}$$

$$\beta cos\theta = 4\varepsilon sin\theta + \frac{k\lambda}{D} \qquad (2)$$

ε is the induced strain.

The induced strain and crystallite size are calculated using Eqn. (2) by drawing a plot between $\beta cos\theta$ (as ordinate) and $4\varepsilon sin\theta$ (as abscissa) and the plots are shown in Fig. 2(a)–(d). The crystallite size and the strain values of the samples extracted from the linear fits are compiled in Table 1. For all the samples, the crystallite size increased with doping concentration. However, no such trend was observed for the micro-strain in the samples. Nevertheless, it is imperative to note that the micro-strain in un-doped BFO is more than in 3 mol% doped BFO. The micro-strain in these samples could be due to several factors, (i) presence of crystal imperfections like $V_O^{\circ\circ}$(oxygen vacancies) and $V_{Bi}^{\circ\circ}$(Bi vacancies) and (ii) crystal lattice variation due to difference in ionic radii of the dopant and the host matrix.

3.2. FTIR studies

FTIR studies were carried out in all the samples in the wave-number range 400−2000 cm^{-1}. All the compositions (x = 0.00, 0,01, 0.03, 0.05, 0.10) showed five strong peaks at around 445 cm^{-1}, 557 cm^{-1}, 1130 cm^{-1}, 1402 cm^{-1} and 1637 cm^{-1} as shown in Fig. 3. The band observed at 1637 cm^{-1} represents the presence of water molecules adsorbed while the sample was exposed to the external environment. The bands observed at 1402 cm^{-1} and 1130 cm^{-1} show the presence of nitrates trapped within the sample during the synthesis process [34]. Specifically, the fundamental absorption bands observed in the range of 400−600 cm^{-1} confirm the metal-oxygen bonds hence validate the existence of perovskite structure in all the samples [35]. The peaks observed at 557 cm^{-1} and 445 cm^{-1} correspond to stretching vibrations of Fe−O bond and bending vibrations of O−Fe−O bond of FeO_6 octahedral unit. These results are in good agreement with the studies reported by Basu et al. [34]. Additionally, a minute shift in absorption peaks with Co substitution could be attributed to the difference in the Columbic interaction between metal and oxygen ions which arise due to either difference in charges or ionic radii of Fe and Co ions.

3.3. Microstructural studies

Fig. 4 depicts the FESEM micrographs of all the samples. Fig. 4(a) is the micrograph of the un-doped BFO, and the image indicates agglomeration of several smaller grains forming grains of varying
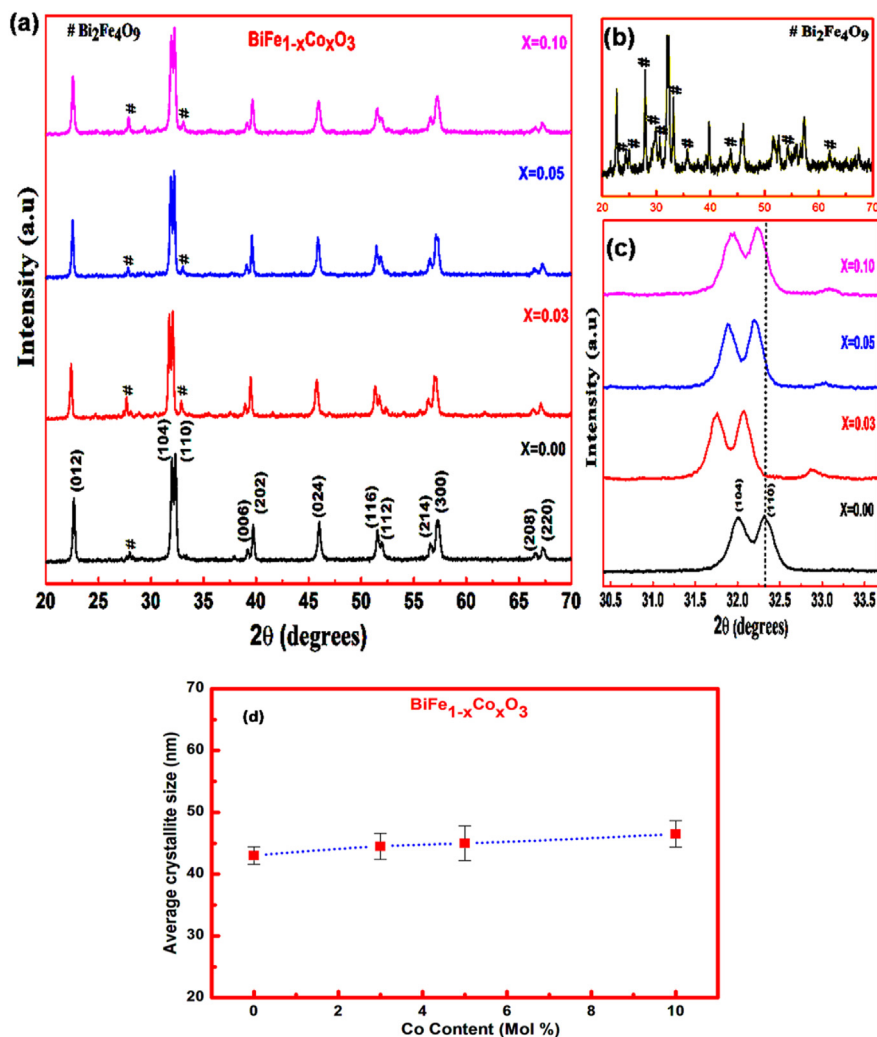
Fig. 1. (a) XRD patterns of different compositions of Co doped BFO (b) XRD pattern of 20 mol% Co doped BFO (c) Magnified view of (104) & (110) crystal planes (d) Crystallite size variation with Co doping concentration.

sizes. With increasing Co doping (Fig. 4b–d) the agglomeration appears to decrease, and for 10 mol% doping, there is a homogeneous distribution of spherical grains which might be attributed to different diffusion rates of the doping ion and host ion. These results suggest a possibility of modifying the granular size and distribution upon Co substitution. Besides, these observations also indicate that higher Co doping concentration leads to a uniformity in the granular shape and size, which could be beneficial for device applications.

3.4. EDAX studies

Energy dispersive x-ray analysis (EDAX) technique enables quantitative compositional analysis of the prepared samples as well as for elemental mapping in different regions of the samples. Fig. 5(a) depicts the EDAX spectrum of pure phase BFO sample while Fig. 5(b)–(d) show the corresponding spectra of Co-doped samples with 3, 5, and 10 mol% of doping concentrations, respectively. These spectra indicate the presence of all elements present in BFO and doped BFO. The spectra also revealed that no foreign elements are present in any of the samples investigated, and importantly all the elements are present in stoichiometric ratios. These ratios were determined by recording the EDAX spectra at

different regions of the samples and taking the average values. Table 2 gives these ratios in terms of atomic percentage. Additionally, the dopant element, namely Co, was detected in all the regions suggesting a uniform distribution of the dopant in the BFO matrix.

3.5. Elemental mapping studies

To further confirm the uniformity of doping across the regions in the sample, elemental mapping studies were carried out in 10 mol% doped Co in BFO. Elemental maps are recorded using the EDAX facility attached to the SEM. Fig. 6 shows the results of elemental mapping studies. A uniform spread in the colors of the elemental maps shown in Fig. 6(a)–(c) indicates the homogeneous distribution of the elements Bi, Fe, and Co in the BFO matrix respectively. However, the patches of dark regions in the map shown in Fig. 6(d) indicate oxygen-deficient regions. Fig. 6(e) shows the mixed mapping image of all the elements. This elemental mapping analysis clearly shows the chemical homogeneity of all the elements present in the BFO matrix and it also lends support to the citrate precursor preparation technique to obtain a uniform distribution of dopants in the BFO matrix.
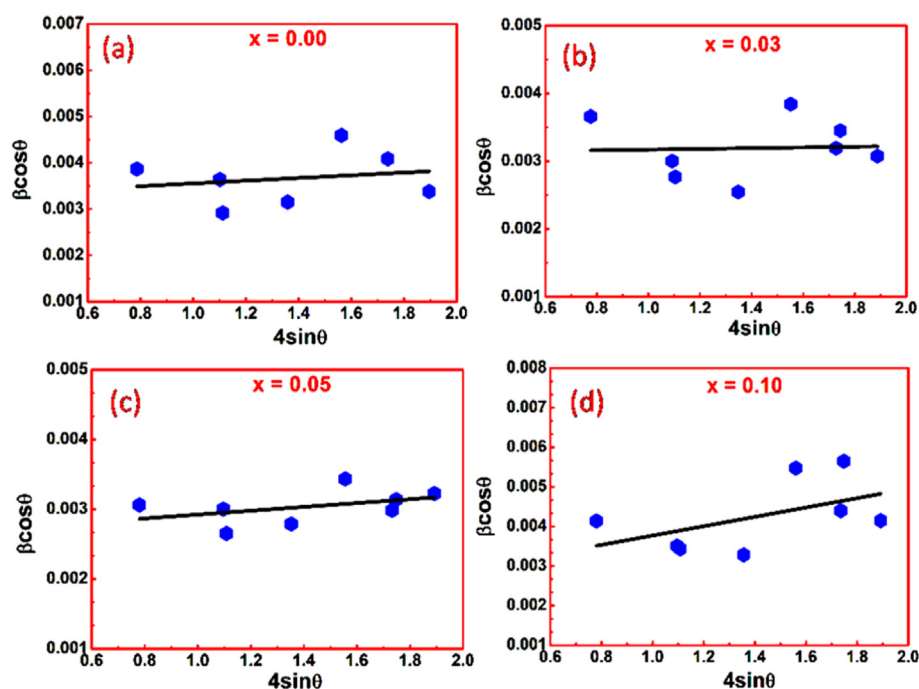
Fig. 2. Williamson-Hall plots of (a) undoped BFO (b) 3 mol% Co-doped BFO (c) 5 mol% Co-doped BFO (d) 10 mol% Co-doped BFO.

Table 1
Average crystallite size and strain of pure BFO and Co doped BFO samples.

Composition	Average crystallite size by Scherrer's method (nm)	Average crystallite size by Williamson−Hall method (nm)	Strain
x = 0.00	43	42	0.00293
x = 0.03	46	44	0.00005
x = 0.05	48	52	0.00274
x = 0.10	49	55	0.00118

3.6. XPS studies

XPS studies help to understand the oxidation state of constituent elements and oxygen vacancies in the samples. Fig. 7(a−d) show the XPS spectra of Bi, Fe, Co and O elements of 10 mol% Co-doped BFO. Carbon 1s (285.8 eV) peak was taken as the reference level to calibrate the binding energy values. The XPS peaks were deconvoluted using Gaussian curve fitting model to obtain information about different oxidation states present for Co and Fe in the doped BFO matrix. Fig. 7(a) shows the XPS spectrum of Bi 4f, which consists of two peaks 158.6 eV and 163.9 eV corresponding to Bi $4f_{7/2}$ and Bi $4f_{5/2}$, respectively. These peaks are consistent with the Bi^{3+} state in BFO as reported in the literature [36,37]. The spectrum for Fe 2p is depicted in Fig. 7(b). It shows two binding energy peaks corresponding to $2p_{3/2}$ and $2p_{1/2}$ at 710.2 eV and 723.7 eV, respectively [36]. In addition to the main peaks, satellite peaks were also observed for the Fe $2p_{1/2}$ binding energy state. Furthermore, Gaussian curve fitting model revealed the presence of Fe^{2+} and Fe^{3+} oxidation states. The binding energy corresponding to these oxidation states is indicated in Fig. 7(b). Fig. 7(c) shows the peaks corresponding to Co $2p_{3/2}$ and Co $2p_{1/2}$ located at 780.7 eV and 796.5 eV, respectively. The splitting of the peaks indicates the presence of Co in both Co^{3+} and Co^{2+} oxidation states [38]. As depicted in Fig. 7(d), the O 1s XPS binding energy peak splits into two sub-peaks appearing at 529.3 eV and 530.8 eV. The peak observed at 529.3 eV corresponds to oxygen-metal bond, whereas the peak at 530.8 eV could be attributed to oxygen defect states, which might be either a vacancy or a dangling bond [36].

Furthermore, the concentration of oxygen defects in Co-doped BFO was found to be more than that of un-doped one (as revealed by the area under the peaks) and hence confirms the fact that Co substitution yields more oxygen vacancies.

3.7. Optical studies

From earlier investigations, it appears that doping of the BFO matrix with transition elements such as Co, Cr, Mn, and Ni have a significant influence on the optical properties of the BFO matrix. In particular, the concentration of dopants was seen to either increase or decrease the optical bandgap in BFO with doping concentration. Therefore, to understand the influence of Co substitution on the optical absorption of BFO samples, synthesized in this work, the UV−visible spectra of both un-doped and cobalt doped samples were recorded. Fig. 8(a) depicts the optical absorbance spectra of the samples recorded in the wavelength range from 350 nm to 800 nm. The figure shows that the optical absorbance for all the samples peak at about 500 nm. Furthermore, the decrease in the absorbance above 600 nm is steeper for the un-doped BFO. The absorption coefficient (α) at 480 nm is calculated using Eqn. (3),

$$\alpha = 2.303 \frac{A}{t} \tag{3}$$

where α is the absorption coefficient, **A** is the absorbance and **t** is the thickness of the sample. The absorption coefficient increases with an increase in Co concentration, as shown in Fig. 8(b). The
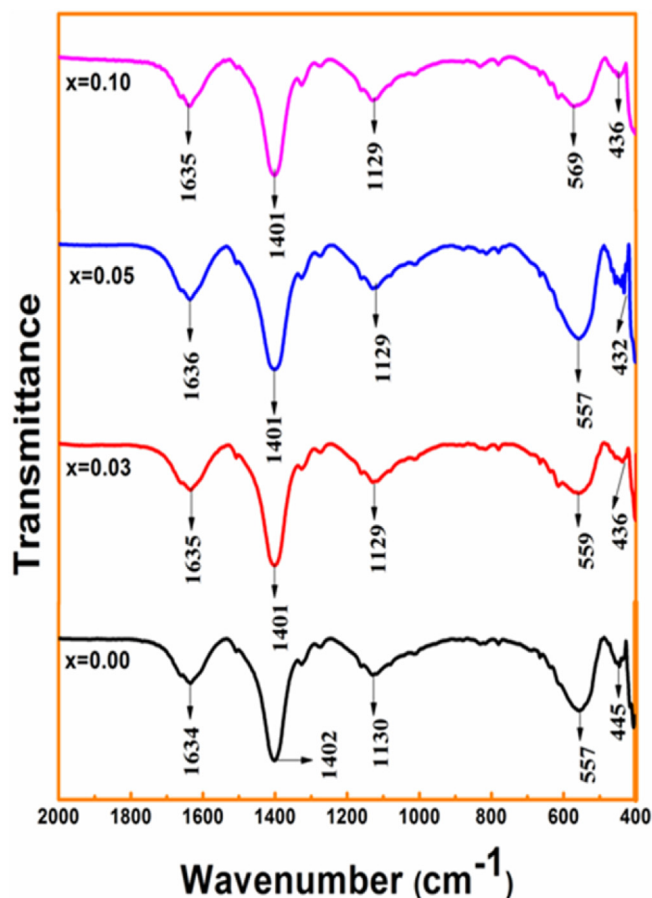
Fig. 3. FTIR spectra of composition $BiFe_{1-x}Co_xO_3$ with x = 0.00, 0.03, 0.05, 0.10.

10 mol% Co-doped BFO exhibits the highest absorption coefficient (~2.00×10^3 cm^{-1}) and this value is 35% more than that of the un-doped sample. This observation suggests Co doping as a better candidate for improving the light-harvesting efficiency (LHE), which is measured by using Eqn. (4), [19].

$$LHE = 1 - 10^{-a} \tag{4}$$

The optical bandgap (OBG) of all the samples is calculated using the Tauc's relation as given by Eqn. (5) [17−19].

$$\alpha h\nu = C(h\nu - E_g)^n \tag{5}$$

where α is the absorption coefficient, h is Planck's constant, ν is the frequency of the incident light, E_g is bandgap, B is energy independent coefficient of absorption frequency, and n is a transition dependent index which is ½ for direct transitions and 2 for indirect transitions. To calculate the OBG values, we considered BFO as a direct bandgap material and plotted $(\alpha h\nu)^2$ as a function of incident photon energy ($h\nu$). Finally, the linear extrapolation of the tangent line to $(\alpha h\nu)^2 = 0$ corresponds to the direct bandgap value of the sample [19]. The direct bandgap value of the un-doped sample was found to be 2.08 ± 0.02 eV, which is in good agreement with the existing data [18,39,40]. A significant reduction in bandgap values was observed with an increase in the Co doping concentration as shown in Fig. 9(a). This reduction in the bandgap is consistent with the observations reported in recent work in Co-doped BFO. To date, several studies have been carried out for tailoring the OBG via chemical substitution. Recently Rhaman et al. tailored the bandgap

of BFO via Co substitution from 2.1 eV to 1.6 eV [18]. Kuang et al. were successful in reducing the bandgap of nanoceramics of BFO from 2.08 eV to 1.70 eV with chemical substitution at A and B site of BFO lattice [17]. They also reported the minimum bandgap of 1.70 eV in the case of Ho and Co-doped samples. Sharmila et al. have also reported an increment of 28% of the light absorption coefficient in the case of Co-doped BFO thin films [19]. Alok et al. tuned the bandgap of BFO nanoparticles from 2.2 eV to 1.7 eV via Co-doping of Gd and Co at A and B sites respectively [41]. These results are indicative of the generation of mid-gap energy states by chemical substitution. The reduced bandgap might also be attributed to induced distortion in Fe−O octahedron and redistribution of molecular orbitals. In the current study, we synthesized Co-doped samples with different Co concentrations at low temperatures and investigated its effect on OBG. The OBG of the 10 mol% doped sample was found to be the least (1.63 ± 0.02 eV) which is 27% lesser than that of un-doped BFO. The variation of the OBG as a function of doping concentration is plotted in Fig. 9(b). The OBG decreases with increasing cobalt doping concentrations.

The possible mechanisms responsible for the variation of OBG with doping in BFO have not been discussed in detail in the literature. Therefore, we provide some arguments that support the variation of OBG in BFO with Co doping. The OBG in BFO is determined by measuring the energy gap between the bottom of Fe (3d) conduction band and the top of the mixed-valence band of O(2p)− Fe(3d) [41]. Therefore, a small distortion of the FeO_6 octahedral could alter the OBG values significantly. Doping of Co at the Fe site leads to this distortion due to the size mismatch of the dopant and host ions and subsequently, the rearrangements of the molecular orbitals might have changed the OBG. Furthermore, the reduction in the OBG with Co doping, as shown in Fig. 9, reveals the presence of defect levels in the forbidden region. This observation suggests either a shift in the acceptor level below the actual conduction band or shift in the donor levels above the original valence band. The other possible reason for the reduction in OBG values is the increase in the concentration of the oxygen vacancies with increasing Co concentration. The increase in the oxygen vacancies with Co doping is supported by the XPS spectra. With doping, Co^{2+} takes Fe^{3+} site in BFO lattice generating more oxygen vacancies for charge compensation and this could be represented by the Kroger-Vink notation,

$$2CoO \rightarrow 2Co'_{Fe} + 2O_o + V_o{}^{\circ\circ}$$
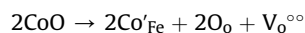
Several experimental results and DFT (density functional theory) calculations have revealed a reduction in OBG with increasing oxygen vacancy concentrations [42−44]. Oxygen vacancies can affect the OBG in two ways; (i) formation of impurity levels between the valence and conduction band and (ii) creation of defective dipole that distorts the O(2p)−Fe(3d) orbital mixing. The reduction in the OBG with increased oxygen vacancies could also be explained from the Boltzmann equation.

$$ni = pi = \sqrt{Nc\,N\nu}\; X \exp\left(-\frac{E_g}{2k_BT}\right) \tag{6}$$

In Eqn. (6), N_C and N_V are the density of states at the conduction and valence band respectively, and E_g is the OBG. Eqn. (6) suggests that the number density of free carriers in the BFO matrix increases with the Co doping. Therefore, Eqn. (6) implies that the OBG has to reduce at a given temperature with Co doping. To conclude this discussion, the other parameters which influence OBG of material include microstructure defects, particle size, and chemical structure [44,45]. In the case of BFO, the presence of a secondary phase of $Bi_2Fe_4O_9$ might also result in OBG reduction as this material has low bandgap (1.6 eV−1.9 eV) [46,47].
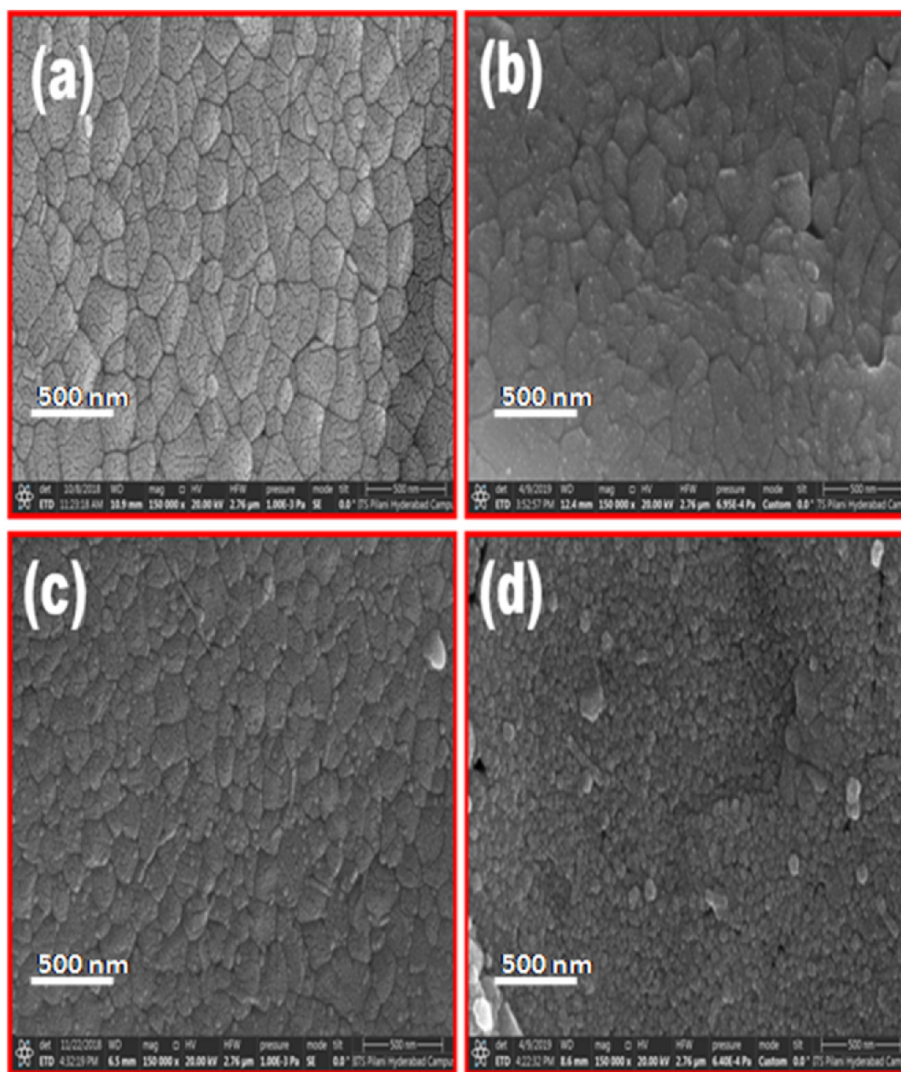
Fig. 4. FESEM micrographs of (a) undoped BFO (b) 3 mol% Co doped BFO (c) 5 mol% Co-doped BFO (d) 10 mol% Co-doped BFO.

3.8. Dielectric studies

The room temperature dielectric properties are measured in the frequency range from 100 Hz to 100 kHz. These measurements used densified pellets. The density of these pellets varied between 89% and 93% of the density of BFO. The real part of the dielectric constant is calculated using the equation $\varepsilon' = \frac{Cd}{A\varepsilon_0}$, Where C is the capacitance measured using the LCR meter, d is the thickness of the sample (0.8 mm < d < 1.2 mm) and A is the area of cross-section of the sample. The imaginary part is calculated using the equation $D = \frac{\varepsilon''}{\varepsilon'}$, where D is the loss factor measured by the LCR meter. Fig. 10(a) shows the real part of the dielectric constant (ε') plotted versus $\log_{10}\omega$ for all the samples. The values of ε' decrease with an increase in frequency and plateaus down to nearly fixed values for frequencies greater than 10 kHz for all the samples. For frequencies below 10 kHz, ε' exhibits dispersion, and the values increase with doping concentration. However, for the Co concentration of 3 mol%, the values of ε' are lesser than the un-doped BFO.

Fig. 10(b) depicts the dielectric loss factor (D) for all the samples. In the frequency range from about 2000 Hz to 20 kHz, D shows dispersion. At frequencies above and below this frequency range, D tends to acquire constant values for all the samples. There appears to be a decrease in D with an increase in frequency and seems to be independent at frequencies higher than ~20 kHz for all the samples studied. These results are in good agreement with reported literature [48−50]. The dielectric loss factor displayed similar behavior to that of ε'. The dielectric losses vanish exponentially in the frequency range of 100 Hz to 20 kHz. The values of D depend on several factors, such as the concentration of Fe^{2+} ions and Co^{2+} ions, stoichiometry, and structural homogeneity, which in turn depends on composition and annealing temperature of material [48,50]. According to Koop's theory, at lower frequencies, the grain boundaries offer higher resistivity (which are more in Co-doped samples), thus making electron flow complicated and hence relatively large amount of energy is required for electron exchange between multivalence states of atoms such as $Co^{2+} \leftrightarrow Co^{3+}$, resulting in higher dielectric loss [51]. Whereas at higher frequencies, which offer lower resistivity, a small amount of energy is required for such electron transfer between multi-valence states and hence results in a low dielectric loss at higher frequencies. However, it appears from Fig. 10(b) that the grain boundary resistivity is extremely high below 2000 Hz, such that there is no electron transfer, and hence the slope appears to be constant.

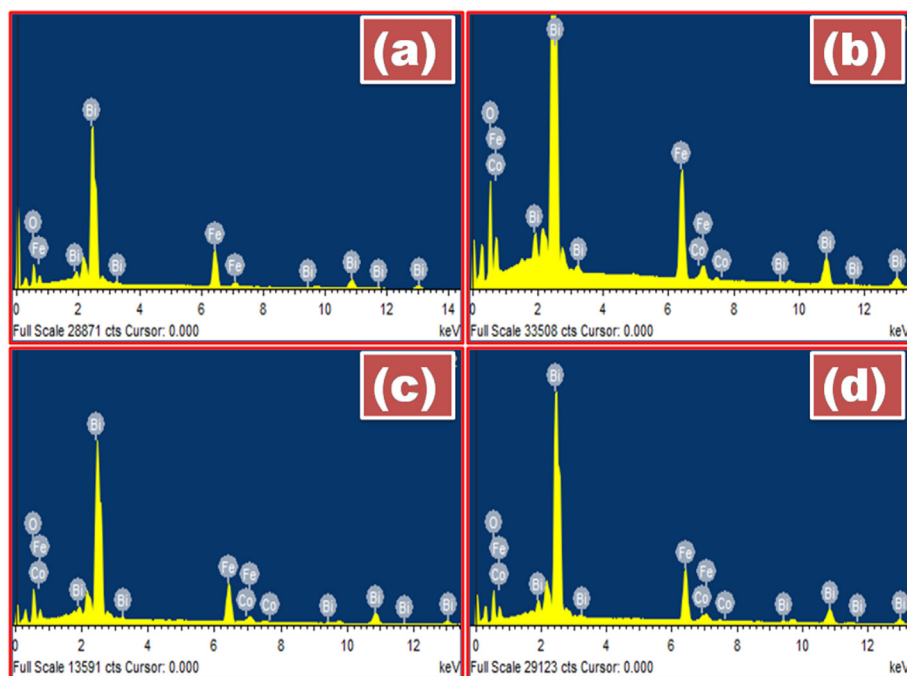The dielectric dispersion at lower frequencies is due to the

Fig. 5. EDAX spectra of (a) undoped BFO (b) 3 mol% Co-doped BFO (c) 5 mol% Co-doped BFO (d) 10 mol% Co-doped BFO.

Table 2
Quantitative elemental composition of all the samples.

Composition	Atomic %			
	Bi	Fe	O	Co
x = 0.00	19.86	20.15	59.99	0.00
x = 0.03	19.93	18.88	60.67	0.52
x = 0.05	20.87	18.11	59.89	1.13
x = 0.10	20.20	18.12	59.64	2.04

dielectric relaxation of electric dipoles. At lower frequencies, the dipoles get enough time to align themselves along the applied electric field and hence can follow the field. However, at higher frequencies, the dipoles cannot follow the oscillating field resulting in a delayed response as reflected in the lower values of ε'. The nearly constant value of ε' above 10 kHz for all the samples is due to the contribution of several polarizations at different stages of measurement. At lower frequencies, all types of polarizations
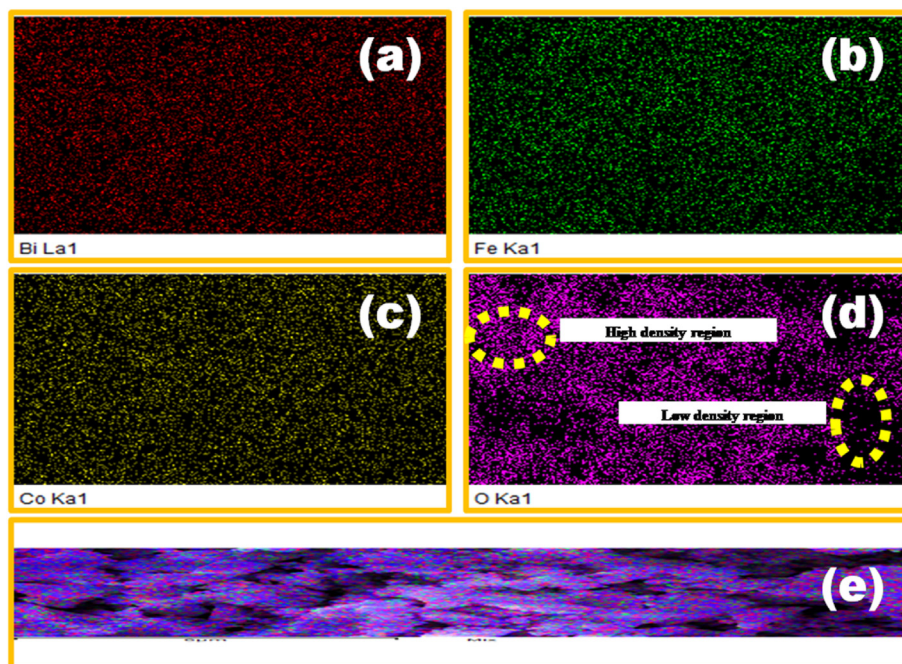

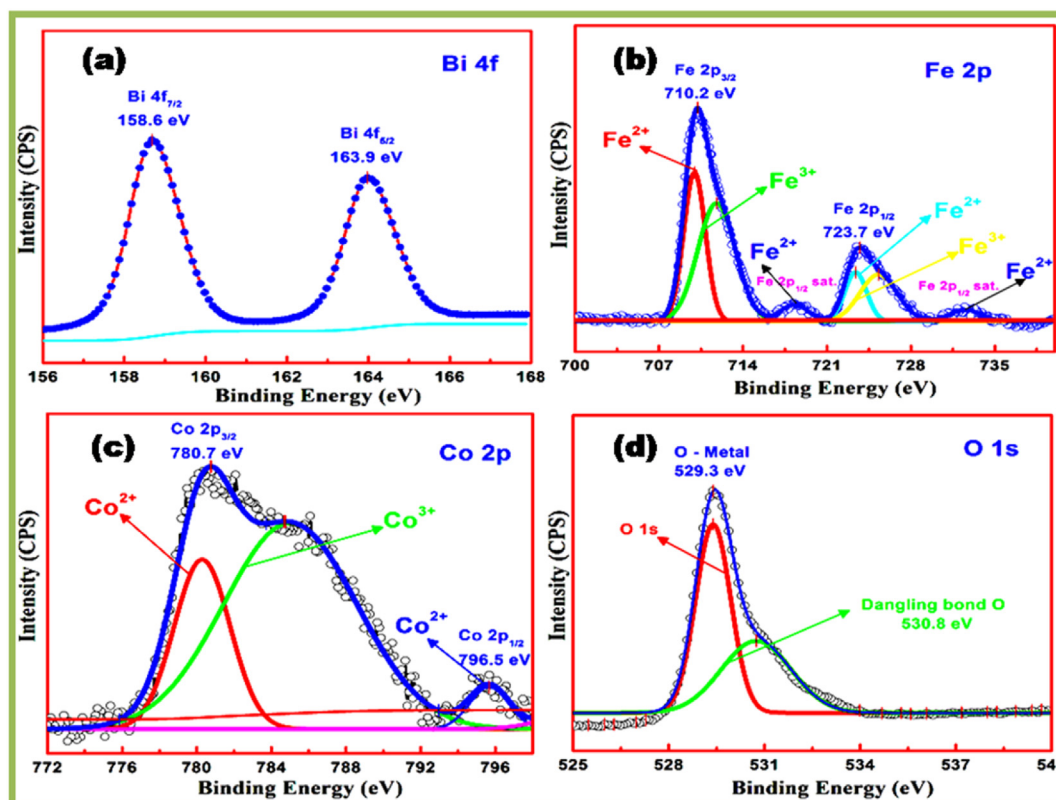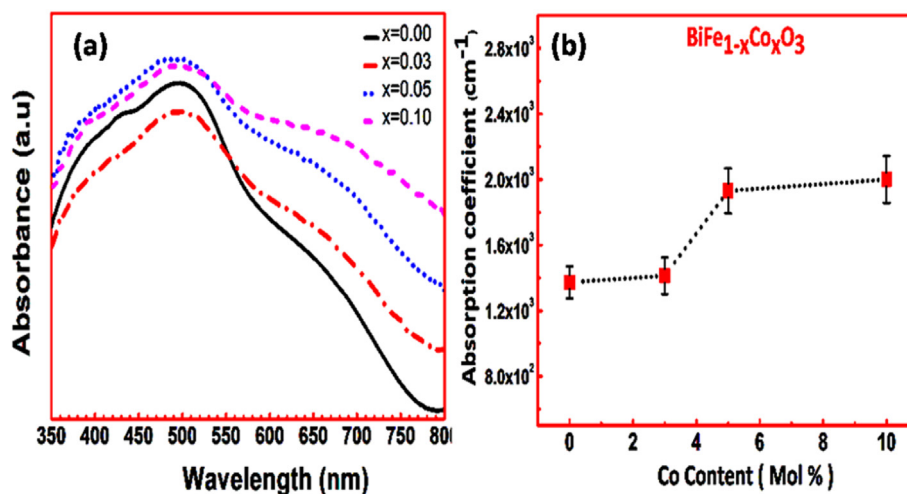**Fig. 6.** Elemental mapping images of (a) Bi (b) Fe (c) Co (d) O (e) all constituent elements.

Fig. 7. Gaussian fitted XPS spectra of (a) Bi (b) Fe (c) Co (d) O.

Fig. 8. (a) Absorbance spectra of composition BiFe1-xCoxO3 with x = 0.00, 0.03, 0.05, 0.10 (b) Absorption coefficient as a function of Co concentration.

contribute, which include electronic, ionic, dipolar and space charge polarization. However, as the frequency is increased, certain polarizations with larger relaxation time cease to contribute, and only those with lower relaxation times contribute, and hence ε' decreases and seems to achieve a constant value above 10 kHz. The higher value of ε' at lower frequency arises due to several factors, including oxygen vacancies, interfacial dislocations, and grain boundaries. An increase in the concentration of grain boundaries (which act as highly resistive media and are more effective at lower frequencies as per Koop's theory) increases the value of ε' [51]. As clearly visible from the SEM micrographs, the microstructures of

these materials consist of inhomogeneous grains and grain boundaries; hence their dielectric behavior can be correlated with space charge polarization. The concentration of grain boundaries increases with doping concentration due to the lattice mismatch between $BiFeO_3$ and $BiCoO_3$, which might be the reason for the enhanced values of ε'.

The ε' values plotted as a function of Co concentration, measured at 20 kHz is depicted in Fig. 10(c). The dielectric behavior with Co doping is also explained in terms of crystallite size, oxygen vacancies, displacement of Fe^{3+} ions, and the presence of Fe^{2+} ions. The role played by each of these factors on ε' is discussed herewith.
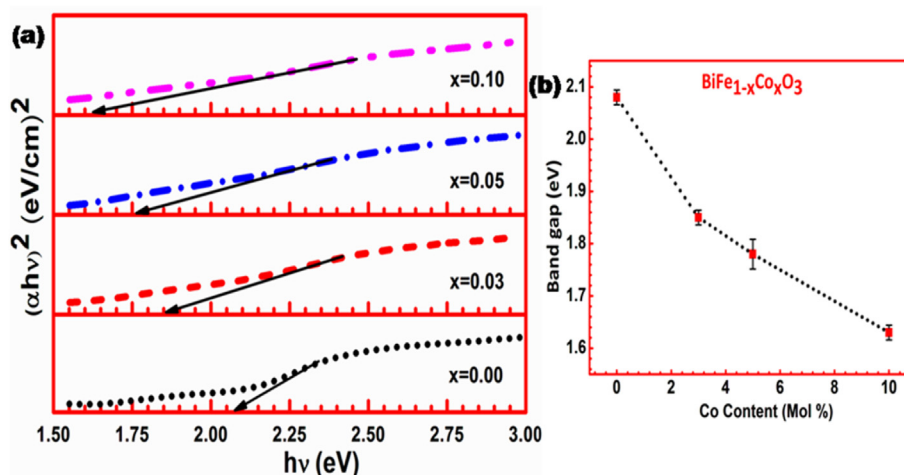
Fig. 9. (a) Represents the Tauc's plots to extract the optical bandgap of compositions BiFe1-xCoxO$_3$ with x = 0.00, 0.03, 0.05, 0.10 (b) Variation of bandgap with Co concentration.

Oxygen vacancies are always presents in pure phase BFO leading to higher conductivity and therefore resulting in smaller dielectric constant. The substitution of Co at Fe site in BFO generates oxygen vacancies and, therefore, reduces the dielectric constant.

It is well known that multiferroic materials, show "size effect" which implies that the physical properties of these materials are size dependent and show different behaviour from a single crystal. However, in our case there are several causes for the non-monotonic behaviour of dielectric values and hence it is difficult to figure out the true size effect from other factors that change the dielectric values within the system. Several reports in literature have shown an increase in dielectric constant values with increase in crystallite size, which is in a good agreement with our studies. This enhancement in dielectric constant values might be attributed to several factors which include the density of the samples and domain wall density. Additionally, it is believed that when the grain size is uniform, the domain wall movement is relatively easy and regular, and dielectric constant increases. In our case, with Co doping the particle size increases and appears to be more uniform than the undoped one and hence the dielectric constant increase.

Furthermore, the increase in Co doping increases the cell volume as the ionic radius of Co^{2+} is larger than that of Fe^{3+} ion and hence increases the free volume available for Fe^{3+} displacement in Fe−O octahedron leading to an increase in the dielectric constant value. However, at a lower concentration of Co (3 mol%), the oxygen vacancies dominate and hence reduce the dielectric constant values. These results are in good agreement with Williamson-Hall's studies. As clearly expressed in Williamson's Hall plots, the samples with x = 0.03 showed the least value of strain, and further increase in doping concentration induced more strain, hence more distortion, which might be the reason for uneven variation in ε′ values with doping concentration.

A small increment in ε′ with higher doping concentration (more than 5 mol%) might be also due to the formation of defective dipoles. As discussed earlier, the charge compensation in the 2$^+$ oxidized ion-doped BFO can be achieved by following mechanisms: (1) creation of oxygen vacancies and (2) increasing cation valence, i.e., conversion of Fe^{2+}−Fe^{+3} (or Fe^{3+}−Fe^{4+} which is not highly probable due to instability issue of Fe^{4+}). Thus Co substitution is expected to suppress the formation of Fe^{2+}. On the other hand, oxygen vacancy may result in the creation of defective dipole ([(Co^{2+})′−(V$_o^{2-}$)$^{\circ\circ}$], which act as capacitors and hence may enhance the dielectric properties. Besides these, defect dipoles restrict the mobility of oxygen vacancies, thus reduce conductivity and

enhance dielectric constant. In addition to this, we have also calculated the bond-strength using Pauling's equation which correlates the bond-strength with the electronegativity of cations and anions of a molecule. Pauling's equation is given as:

$$I_{CA} = 1 - \exp\frac{-|X_c - X_A|}{4} \tag{7}$$

where I_{CA} is cation-anion bond-strength, X_C and X_A are electronegativities of cation and anion, respectively. In BFO material A and B sites carry cations, and O is the anion. In co-doped BFO, Co and Fe ions are the B-site cations, and O is the anion. The oxidation states of Co, Fe and O were considered as 2+, 3+ and 2- respectively, hence their respective electronegativity values were taken as 0.32, 0.33, and 3.44 accordingly. The calculated bond-strength value of Co−O bond is higher than that of Fe−O bond and was found to be 0.542 and 0.540, respectively, as calculated using Eqn. (7). This difference in the ionic bond-strengths might be the reason for the slight variation in dielectric behaviour of our samples.

4. Conclusions

In summary, we have synthesized BiFe$_{1-x}$Co$_x$O$_3$ with (x = 0.00, 0.03, 0.05, 0.10) nanoceramic samples using a modified sol-gel citrate precursor technique with water as the solvent. This preparation technique appears to have reduced the formation of the undesirable secondary phase. All investigated samples showed a perovskite structure and the average crystallite size increased with increasing doping concentration. The induced strain decreased initially and then enhanced with the increase in doping concentration. The grain size increased with Co doping, and with further increase in doping (x = 0.10), the grain shape changed from granular to spherical. All samples show a uniform distribution of dopants. XPS results indicated the enhanced concentration of oxygen vacancies due to cobalt substitution; thus, Co substitution provides a pathway for generating more oxygen vacancies. The dielectric properties (real part) initially decreased to 3 mol% Co-doped and then increased with increasing doping concentration (≥5 mol%). The Co substitution enhanced the absorption coefficient by 35% compared to that of un-doped BFO measured at a wavelength of 480 nm. The optical bandgap decreased (from 2.08 ± 0.02 eV to 1.63 ± 0.02 eV) with Co substitution without deteriorating the essential structural characteristics of BFO material. The present investigations indicate that the conditions for the synthesis of BFO
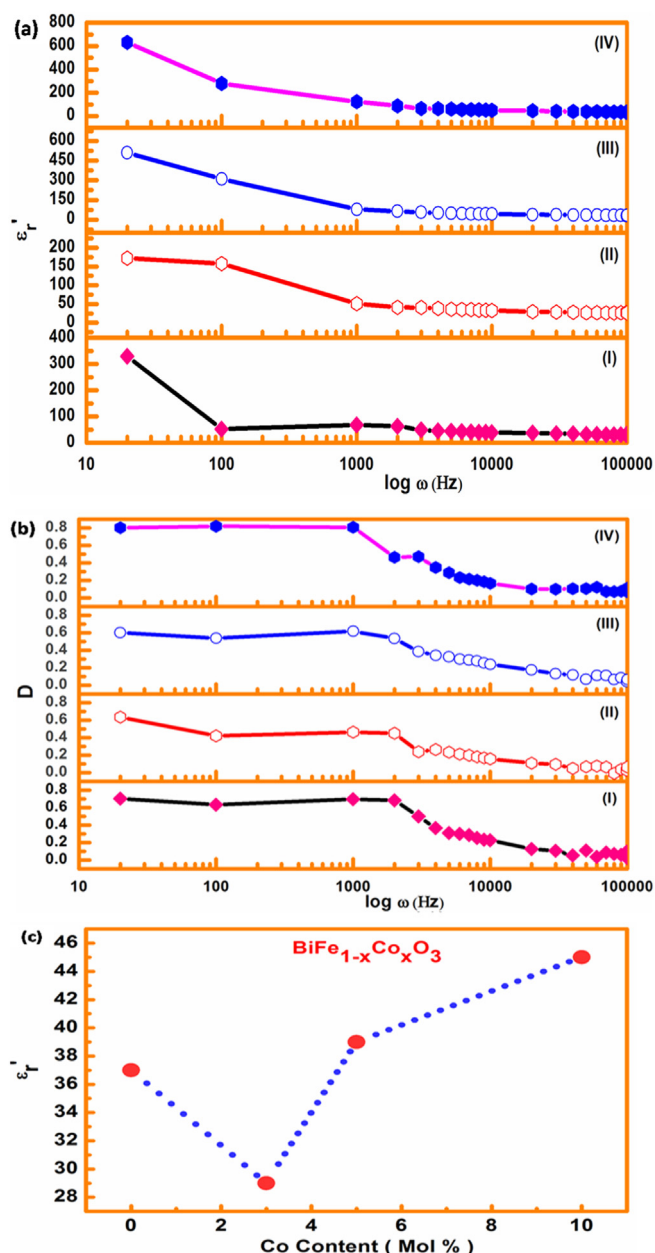
Fig. 10. (a) Dielectric constant as a function of frequency for (I) undoped BFO (II) 3 mol % Co-doped BFO (III) 5 mol% Co-doped BFO (IV) 10 mol% Co-doped BFO, (b) Dielectric loss factor as a function of frequency for (I) undoped BFO (II) 3 mol% Co-doped BFO (III) 5 mol% Co-doped BFO (IV) 10 mol% Co-doped BFO (c) Dielectric constant values at 20 kHz with doping concentration.

need to be carefully optimized so that the presence of undesirable secondary phase formations can be reduced or eliminated. The reduction of optical bandgap with cobalt doping suggests that optimally doped BFO is a promising candidate for light-harvesting applications. However, more investigations are necessary to prepare un-doped/doped BFO on a large scale with less leakage current densities to replace the conventional materials for photovoltaic applications.

CRediT authorship contribution statement

Waseem Ahmad Wani: Conceptualization, Methodology, Investigation, Writing - original draft, Formal analysis. **Souvik**

Kundu: Writing - review & editing. **Kannan Ramaswamy:** Writing - review & editing. **Harihara Venkataraman:** Writing - review & editing, Supervision.

Declaration of competing interest

The authors declare that they have no known competing financial interests or personal relationships that could have appeared to influence the work reported in this paper.

Acknowledgement

References

[1] R. Ramesh, N.A. Spaldin, Multiferroics: progress and prospects in thin films, Nat. Mater. 6 (1) (2007) 21−29, https://doi.org/10.1038/nmat1805.
[2] C. Ederer, N.A. Spaldin, Weak ferromagnetism and magnetoelectric coupling in bismuth ferrite, Phys. Rev. B 71 (6) (2005), https://doi.org/10.1103/PhysRevB.71.060401, 060401.
[3] P. Fischer, M. Polomska, I. Sosnowska, M. Szymanski, Temperature dependence of the crystal and magnetic structures of $BiFeO_3$, J. Phys. C Solid State Phys. 13 (10) (1980) 1931, https://doi.org/10.1088/0022-3719/13/10/012.
[4] B. Ruette, S. Zvyagin, A.P. Pyatakov, A. Bush, J.F. Li, V.I. Belotelov, A.K. Zvezdin, D. Viehland, Magnetic-field-induced phase transition in $BiFeO_3$ observed by high-field electron spin resonance: cycloidal to homogeneous spin order, Phys. Rev. B 69 (6) (2004), https://doi.org/10.1103/PhysRevB.69.064114, 064114.
[5] J.B. Neaton, C. Ederer, U.V. Waghmare, N.A. Spaldin, K.M. Rabe, First-principles study of spontaneous polarization in multiferroic$BiFeO_3$, Phys. Rev. B 71 (1) (2005), https://doi.org/10.1103/PhysRevB.71.014113, 014113.
[6] R. Haumont, I.A. Kornev, S. Lisenkov, L. Bellaiche, J. Kreisel, B. Dkhil, Phase stability and structural temperature dependence in powdered multiferroic$BiFeO_3$, Phys. Rev. B 78 (13) (2008) 134108, https://doi.org/10.1103/PhysRevB.78.134108.
[7] B.K. Vashisth, J.S. Bangruwa, A. Beniwal, S.P. Gairola, A. Kumar, N. Singh, V. Verma, Modified ferroelectric/magnetic and leakage current density properties of Co and Sm co-doped bismuth ferrites, J. Alloys Compd. 698 (2017) 699−705, https://doi.org/10.1016/j.jallcom.2016.12.278.
[8] Y. Wang, C.W. Nan, Effect of Tb doping on electric and magnetic behavior of $BiFeO_3$thin films, J. Appl. Phys. 103 (2) (2008), https://doi.org/10.1063/1.2831026, 024103.
[9] S.K. Singh, Structural and electrical properties of Sm-substituted $BiFeO_3$ thin films prepared by chemical solution deposition, Thin Solid Films 527 (2013) 126−132, https://doi.org/10.1016/j.tsf.2012.11.062.
[10] F. Yan, M.O. Lai, L. Lu, T.J. Zhu, Enhanced multiferroic properties and valence effect of Ru-doped $BiFeO_3$ thin films, J. Phys. Chem. C 114 (15) (2010) 6994−6998, https://doi.org/10.1021/jp1009127.
[11] H. Yan, H. Deng, N. Ding, J. He, L. Peng, L. Sun, P. Yang, J. Chu, Influence of transition elements doping on structural, optical and magnetic properties of $BiFeO_3$ films fabricated by magnetron sputtering, Mater. Lett. 111 (2013) 123−125, https://doi.org/10.1016/j.matlet.2013.08.075.
[12] H. Naganuma, J. Miura, S. Okamura, Ferroelectric, electrical and magnetic properties of Cr, Mn, Co, Ni, Cu added polycrystalline $BiFeO_3$ films, Appl. Phys. Lett. 93 (5) (2008), https://doi.org/10.1063/1.2965799, 052901.
[13] T. Kawae, Y. Terauchi, H. Tsuda, M. Kumeda, A. Morimoto, Improved leakage and ferroelectric properties of Mn and Tico-doped $BiFeO_3$ thin films, Appl. Phys. Lett. 94 (11) (2009) 112904, https://doi.org/10.1063/1.3098408.
[14] X. Qi, J. Dho, R. Tomov, M.G. Blamire, J.L. MacManus-Driscoll, Greatly reduced leakage current and conduction mechanism in aliovalent ion doped $BiFeO_3$, Appl. Phys. Lett. 86 (6) (2005), 062903, http://link.aip.org/link/doi/10.1063/1.1862336.
[15] S. Yang, F. Zhang, X. Xie, X. Guo, L. Zhang, S. Fan, Effects of transition metal (Cu, Zn, Mn) doped on leakage current and ferroelectric properties of $BiFeO_3$ thin films, J. Mater. Sci. Mater. Electron. 28 (20) (2017) 14944−14948, https://doi.org/10.1007/s10854-017-7366-8.
[16] T. Choi, S. Lee, Y.J. Choi, V. Kiryukhin, S.W. Cheong, Switchable ferroelectric diode and photovoltaic effect in $BiFeO_3$, Science 324 (5923) (2009) 63−66, https://doi.org/10.1126/science.1168636.
[17] D. Kuang, F. Yang, W. Wang, Z. Yang, Effects of Ho^{3+} and transition metal ion doping on optical and magnetic properties of $BiFeO_3$nanopowders, J. Mater.

Sci. Mater. Electron. 29 (5) (2018) 4041−4047, https://doi.org/10.1007/s10854-017-8347-7.

[18] M.M. Rhaman, M.A. Matin, M.N. Hossain, F.A. Mozahid, M.A. Hakim, M.F. Islam, Bandgap engineering of cobalt-doped bismuth ferrite nanoparticles for photovoltaic applications, Bull. Mater. Sci. 42 (4) (2019) 190, https://doi.org/10.1007/s12034-019-1871-8.

[19] M. Sharmila, S.A. Kader, D.J. Ruth, M.V.G. Babu, B. Bagyalakshmi, R.A. Kumar, D.P. Padiyan, B. Sundarakannan, Effect of cobalt substitution on the optical properties of bismuth ferrite thin films, Mater. Sci. Semicond. Process. 34 (2015) 109−113, https://doi.org/10.1016/j.mssp.2015.01.047.

[20] M.M. Rashad, Effect of synthesis conditions on the preparation of BiFeO3 nanopowders using two different methods, J. Mater. Sci. Mater. Electron. 23 (4) (2012) 882−888, https://doi.org/10.1007/s10854-011-0513-8.

[21] C.J. Tsai, C.Y. Yang, Y.C. Liao, Y.L. Chueh, Hydrothermally grown bismuth ferrites: controllable phases and morphologies in a mixed KOH/NaOH mineralizer, J. Mater. Chem. 22 (34) (2012) 17432−17436, https://doi.org/10.1039/C2JM33859A.

[22] Y.P. Wang, L. Zhou, M.F. Zhang, X.Y. Chen, J.M. Liu, Z.G. Liu, Room-temperature saturated ferroelectric polarization in BiFeO3 ceramics synthesized by rapid liquid phase sintering, Appl. Phys. Lett. 84 (10) (2004) 1731−1733, https://doi.org/10.1063/1.1667612.

[23] M.M. Kumar, V.R. Palkar, K. Srinivas, S.V. Suryanarayana, Ferroelectricity in a pure BiFeO3 ceramic, Appl. Phys. Lett. 76 (19) (2000) 2764−2766, https://doi.org/10.1063/1.126468.

[24] S.K. Singh, Y.K. Kim, H. Funakubo, H. Ishiwara, Epitaxial BiFeO3 thin films fabricated by chemical solution deposition, Appl. Phys. Lett. 88 (16) (2006) 162904, https://doi.org/10.1063/1.2196477.

[25] D.C. Jia, J.H. Xu, H. Ke, W. Wang, Y. Zhou, Structure and multiferroic properties of BiFeO3 powders, J. Eur. Ceram. Soc. 29 (14) (2009) 3099−3103, https://doi.org/10.1016/j.jeurceramsoc.2009.04.023.

[26] S.H. Xie, J.Y. Li, R. Proksch, Y.M. Liu, Y.C. Zhou, Y.Y. Liu, Y. Ou, L.N. Lan, Y. Qiao, Nanocrystalline multiferroic BiFeO3 ultrafine fibers by sol-gel based electrospinning, Appl. Phys. Lett. 93 (22) (2008) 222904, https://doi.org/10.1063/1.3040010.

[27] D. Maurya, H. Thota, K.S. Nalwa, A. Garg, BiFeO3 ceramics synthesized by mechanical activation assisted versus conventional solid-state-reaction process: a comparative study, J. Alloys Compd. 477 (1−2) (2009) 780−784, https://doi.org/10.1016/j.jallcom.2008.10.155.

[28] J.H. Xu, H. Ke, D.C. Jia, W. Wang, Y. Zhou, Low-temperature synthesis of BiFeO3 nanopowders via a sol−gel method, J. Alloys Compd. 472 (1−2) (2009) 473−477, https://doi.org/10.1016/j.jallcom.2008.04.090.

[29] B.L. Cushing, V.L. Kolesnichenko, C.J. O'Connor, Recent advances in the liquid-phase syntheses of inorganic nanoparticles, Chem. Rev. 104 (9) (2004) 3893−3946, https://doi.org/10.1021/cr030027b.

[30] X. Yang, Y. Zhang, G. Xu, X. Wei, Z. Ren, G. Shen, G. Han, Phase and morphology evolution of bismuth ferrites via hydrothermal reaction route, Mater. Res. Bull. 48 (4) (2013) 1694−1699, https://doi.org/10.1016/j.materresbull.2013.01.032.

[31] A. Sagdeo, P. Mondal, A. Upadhyay, A.K. Sinha, A.K. Srivastava, S.M. Gupta, P. Chowdhury, T. Ganguli, S.K. Deb, Correlation of microstructural and physical properties in bulk BiFeO3 prepared by rapid liquid-phase sintering, Solid State Sci. 18 (2013) 1−9, https://doi.org/10.1016/j.solidstatesciences.2012.12.017.

[32] Q.H. Jiang, C.W. Nan, Z.J. Shen, Synthesis and properties of multiferroic La-modified BiFeO3 ceramics, J. Am. Ceram. Soc. 89 (7) (2006) 2123−2127, https://doi.org/10.1111/j.1551-2916.2006.01062.x.

[33] A.K. Zak, W.A. Majid, M.E. Abrishami, R. Yousefi, X-ray analysis of ZnO nanoparticles by Williamson−Hall and size−strain plot methods, Solid State Sci. 13 (1) (2011) 251−256, https://doi.org/10.1016/j.solidstatesciences.2010.11.024.

[34] A. Mukherjee, S.M. Hossain, M. Pal, S. Basu, Effect of Y-doping on optical properties of multiferroic BiFeO3 nanoparticles, Appl. Nanosci. 2 (3) (2012) 305−310, https://doi.org/10.1007/s13204-012-0114-8.

[35] P. Chen, X. Xu, C. Koenigsmann, A.C. Santulli, S.S. Wong, J.L. Musfeldt, Size-dependent infrared phonon modes and ferroelectric phase transition in BiFeO3 nanoparticles, Nano Lett. 10 (11) (2010) 4526−4532, https://doi.org/10.1021/nl102470.

[36] Y. Zhang, Y. Wang, J. Qi, Y. Tian, M. Sun, J. Zhang, T. Hu, M. Wei, Y. Liu, J. Yang, Enhanced magnetic properties of BiFeO3 thin films by doping: analysis of structure and morphology, Nanomaterials 8 (9) (2018) 711, https://doi.org/10.3390/nano8090711.

[37] N. Zhang, D. Chen, F. Niu, S. Wang, L. Qin, Y. Huang, Enhanced visible light photocatalytic activity of Gd-doped BiFeO3 nanoparticles and mechanism insight, Sci. Rep. 6 (1) (2016) 1−11, https://doi.org/10.1038/srep26467.

[38] G. Xiong, P. He, L. Liu, T. Chen, T.S. Fisher, Synthesis of porous Ni−Co−Mn oxide nanoneedles and the temperature dependence of their pseudocapacitive behavior, Front. Energy Res. 3 (2015) 39, https://doi.org/10.3389/fenrg.2015.00039.

[39] F. Gao, X.Y. Chen, K.B. Yin, S. Dong, Z.F. Ren, F. Yuan, T. Yu, Z.G. Zou, J.M. Liu, Visible-light photo-catalytic properties of weak magnetic BiFeO3 nanoparticles, Adv. Mater. 19 (19) (2007) 2889−2892, https://doi.org/10.1002/adma.200602377.

[40] R. Guo, L. Fang, W. Dong, F. Zheng, M. Shen, Enhanced photocatalytic activity and ferromagnetism in Gd doped BiFeO3 nanoparticles, J. Phys. Chem. C 114 (49) (2010) 21390−21396, https://doi.org/10.1021/jp104660a.

[41] A.K. Vishwakarma, P. Tripathi, A. Srivastava, A.S.K. Sinha, O.N. Srivastava, Band gap engineering of Gd and Co doped BiFeO3 and their application in hydrogen production through photoelectrochemical route, Int. J. Hydrogen Energy 42 (36) (2017) 22677−22686, https://doi.org/10.1016/j.ijhydene.2017.07.153.

[42] S. Ju, T.Y. Cai, First-principles studies of the effect of oxygen vacancies on the electronic structure and linear optical response of multiferroic BiFeO3, Appl. Phys. Lett. 95 (23) (2009) 231906, https://doi.org/10.1063/1.3272107.

[43] K. Jiang, J.J. Zhu, J.D. Wu, J. Sun, Z.G. Hu, J.H. Chu, Influences of oxygen pressure on optical properties and interband electronic transitions in multiferroic bismuth ferrite nanocrystalline films grown by pulsed laser deposition, ACS Appl. Mater. Interfaces 3 (12) (2011) 4844−4852, https://doi.org/10.1021/am201340d.

[44] P.S. Mocherla, C. Karthik, R. Ubic, M.S. Ramachandra Rao, C. Sudakar, Tunable bandgap in BiFeO3 nanoparticles: the role of microstrain and oxygen defects, Appl. Phys. Lett. 103 (2) (2013), https://doi.org/10.1063/1.4813539, 022910.

[45] S. Gómez-Salces, F. Aguado, F. Rodríguez, R. Valiente, J. González, R. Haumont, J. Kreisel, Effect of pressure on the band gap and the local FeO6 environment in BiFeO3, Phys. Rev. B 85 (14) (2012) 144109, https://doi.org/10.1103/PhysRevB.85.144109.

[46] Z. Irshad, S.H. Shah, M.A. Rafiq, M.M. Hasan, First principles study of structural, electronic and magnetic properties of ferromagnetic Bi2Fe4O9, J. Alloys Compd. 624 (2015) 131−136, https://doi.org/10.1016/j.jallcom.2014.10.174.

[47] Q. Zhang, W. Gong, J. Wang, X. Ning, Z. Wang, X. Zhao, W. Ren, Z. Zhang, Size-dependent magnetic, photo-absorbing, and photocatalytic properties of single-crystalline Bi2Fe4O9 semiconductor nanocrystals, J. Phys. Chem. C 115 (51) (2012) 25241−25246, https://doi.org/10.1021/jp208750n.

[48] S. Chandel, P. Thakur, M. Tomar, V. Gupta, A. Thakur, Investigation of structural, optical, dielectric and magnetic studies of Mn substituted BiFeO3 multiferroics, Ceram. Int. 43 (16) (2017) 13750−13758, https://doi.org/10.1016/j.ceramint.2017.07.088.

[49] A.D. Sharma, H. Hemanta, H.B. Sharma, Effect of Mn substitution on structural and dielectric properties of bismuth ferrite, Ferroelectrics 519 (1) (2017) 187−193, https://doi.org/10.1080/00150193.2017.1361257.

[50] B. Dhanalakshmi, K. Pratap, B.P. Rao, P.S. Rao, Effects of Mn doping on structural, dielectric and multiferroic properties of BiFeO3 nanoceramics, J. Alloys Compd. 676 (2016) 193−201, https://doi.org/10.1016/j.jallcom.2016.03.208.

[51] I.H. Gul, A. Maqsood, M. Naeem, M.N. Ashiq, Optical, magnetic and electrical investigation of cobalt ferrite nanoparticles synthesized by co-precipitation route, J. Alloys Compd. 507 (1) (2010) 201−206, https://doi.org/10.1016/j.jallcom.2010.07.155.